

Pronounced impact of size and shape effects on creep rupture life of a K439B superalloy combustion chamber casting simulator

Wen-tong Liu¹, Yi-dong Wu¹, Lei Gao¹, Jing-yang Chen², **Cheng-bo Xiao², and *Xi-dong Hui¹

1. State Key Laboratory for Advanced Metals and Materials, University of Science and Technology Beijing, Beijing 100083, China

2. Science and Technology on Advanced High Temperature Structural Materials Laboratory, Beijing Institute of Aeronautical Materials, Beijing 100095, China

Copyright © 2025 Foundry Journal Agency

Abstract: The size and shape effect (SSE) of components has become a critical issue for mechanical properties, application reliability, and processing. In this study, the creep rupture life (CRL) of components with different wall thicknesses and positions in a combustion chamber casing simulator made of K439B superalloy was investigated. The intrinsic mechanisms of the SSE were explored from the dendrite structure, volume fraction and size of the γ' phase, and element segregation, etc. It is shown that this casting exhibits a strong SSE of creep rupture life, characterized by a significant difference in the CRL values up to 60% with the variation of wall thickness and position in the casing. In terms of casting technology, the influence of SSE on CRL is actually determined by the cooling rate. The SSE on the creep rupture life originates from the dendrite structure (such as the secondary dendrite arm spacing), volume fraction size of the γ' phase in the dendrite trunk, and elements segregation rate. This work may have implications for the design and application of engineering components with large sizes and complex structures.

Keywords: K439B superalloy; size and shape effects; creep rupture life; cooling rate; γ' phase; combustion chamber casing simulator

CLC numbers: TG146.175

Document code: A

Article ID: 1672-6421(2025)02-215-07

1 Introduction

The main combustor casing is a key component of turbine engines. Traditionally, the combustor casing is manufactured through a complicated process involving the sheet-metal processing of the internal and external casings, the precision casting of the diffusive casing, and the welding of the three parts. In recent years, the traditional processing technology for the main combustor casing has been simplified to integrated precision casting, which brings significant advantages in reducing the weight of the engine, enhancing the stiffness and high-temperature strength, and lowering the manufacturing cost [1-3]. However, this new technology has presented some challenges, such as the microstructure and

properties of the integrated casing vary significantly at different positions due to the changes in wall thickness, size, and complexity of the casing shape, also known as the size and shape effect (SSE). Even for the positions with the same wall thickness in the casting, the microstructure and properties still differ [4]. In this case, the microstructure and properties of the casing cannot be evaluated solely based on the corresponding properties of the standard samples of alloys. It has been found that thin walls have the greatest impact on the equiaxial crystal castings, with a significant effect on room and high-temperature properties [5-8]. Unfortunately, the SSE has not been adequately considered, forcing engine designers to increase the safety margin to ensure the reliability of the hot-end components. As a result, it is difficult to achieve the goals of the relevance of the structure, weight reduction, and homogeneous mechanical properties of the components.

Superalloys, including nickel, cobalt, and iron-based superalloys, have been rapidly developed for blades, discs, and casings of aeroengines and heavy-duty combustion turbines since the 1940s [9].

*Xi-dong Hui

Professor. Research interest: Cast superalloys and amorphous alloys.

E-mail: xdhui@ustb.edu.cn

**Cheng-bo Xiao

E-mail: cbxiao0288@sina.com

Received: 2023-12-28; Revised: 2024-05-20; Accepted: 2024-08-22

Among them, cast Ni-based superalloys have been widely applied in the manufacture of complex components due to their excellent high-temperature mechanical properties, heat and corrosion resistance, castability, and relatively low cost^[10, 11]. Currently, the most common Ni-based superalloy for complex components is still Inconel 718 alloy^[12, 13], which has outstanding mechanical properties, castability, and weldability below 650 °C. With the increase in the temperature of the gas at the front inlet of the engine, the heat capacity of the main combustor casing is required to be correspondingly enhanced. In this regard, GTD222 (K4222) and Waspaloy nickel-based superalloys have been developed for guide blades and turbine discs operating at 750 °C^[14, 15]. Nimonic C263 (K4163) nickel superalloy has been prepared for igniters and diffusers operating at 800 °C, but its strength was found to be insufficient and η phase was precipitated after aging for several hundred hours^[16]. BX4J-BИ (K4648) superalloy has excellent oxidation and corrosion resistance and has been applied to the diffuser, but its high-temperature strength is relatively low^[17]. Mar-M247 superalloy is innovated for interstage guides at temperatures above 1,000 °C. One of the major drawbacks of Mar-M247 alloy is poor weldability^[18]. In recent years, new cast Ni-based superalloys such as IN939 and CM939 alloys with a heat capacity of up to 800 °C have been developed^[19, 20]. Another novel cast superalloy, named K439B alloy, with excellent high-temperature strength, microstructure stability, and good processing properties, was also innovated by the Beijing Institute of Aeronautical Materials^[21]. This alloy shows promising prospects for large complex components such as combustion casings and gate apparatuses of turbine engines.

So far, many investigations have been carried out on the ambient and high-temperature tensile strength, creep properties, structural stability, and physical and chemical properties of the standard samples of K439B alloy. Chen et al.^[21] reported the microstructure, mechanical properties and microstructural stability after long-term aging at 800 °C of K439B. Men et al.^[22] characterized the microstructure and mechanical properties of laser welded and post-weld heat-treated K439B superalloy. Zhang and Gao et al.^[23, 24] have studied the evolution of the microstructure and mechanical properties of K439B equiaxed superalloy after long-term aging at 800 °C. However, in the casing simulator, the structure and solidification sequence of the casing result in significant variations in creep rupture life (CRL) due to the different wall thicknesses and positions. During the solidification process of the casting, different areas show significantly different cooling rates, which then leads to different microstructures and composition redistribution, and finally causes the obvious difference in CRL. To date, only the CRL of K439B rod specimens has been studied^[21]. The relationship between the wall thickness and shape of the actual casting, which actually affects the solidification process, has not been studied. The internal mechanism of SSE generated by casting structure and phase constitution has not been thoroughly understood. In this work, a combustion chamber

casing simulator that integrated the internal and external casing and diffuser was designed. This casing simulator was manufactured using precision casting method, and was subjected to heat treatment and hot isostatic pressing. CRL at the flange face and in the wall with different thicknesses was studied. An investigation was performed into the effects of varying positions of the simulator on the dendritic microstructure, the volume fraction and size of the γ' phase, as well as the elemental partitioning. The intrinsic mechanism of SSE was discussed in detail. This work is expected to provide a reference for the design and application of combustion casings with large sizes and a complex structure.

2 Experiment and simulation methods

2.1 Design of cast technology of the simulate combustion casing

The outline of the combustion chamber casing simulator is shown in Fig. 1(a). The casing simulator has an uneven wall with the thickest part being 16 mm and the thinnest part being 2.5 mm, along with a complex flange bottom. In order to obtain a homogeneous casting without casting defects, Zheng^[25] from our team optimized the casting technology using the PROCAST software. And the optimized casting technology is shown in Fig. 1(b). For this casting, the gating system, including the downsprue, cross gate, and pouring basin, was set up. Especially, 8 feeding sprues were designed to avoid shrinkage, cavity and porosity^[26].

2.2 Manufacture and heat treatment of casing simulator

The casing simulator was cast using precision casting technology under a vacuum condition. Before pouring, the mold was preheated to 930 °C. The pouring temperature of the melt was 1,520 °C. The pouring was completed in 6 s. Then, the casting was held in the mold until the temperature dropped to 500 °C. The final product of the casting is shown in Figs. 1(c) and (d).

The casting was then heat-treated in an air-conditioned environment with the following parameters: 1,160 °C/4 h+air cooling (AC), 1,080 °C/4 h+AC, and 845 °C/20 h+AC. Finally, the casting was further processed using hot isostatic pressing (HIP) at 1,165 °C for 4 h under 150 MPa.

2.3 Sectioning scheme of the casting

The characteristic size and the range of thickness of the wall in different parts of the casting are shown in Fig. 2. To investigate the microstructure and mechanical properties of different parts of the casting, the sectioning of the casting was carried out, as shown in Fig. 2. Samples were sectioned from 6 areas, named as Areas A, B, C, D, E, and F, respectively. Among them, Areas A and B belong to the thick wall, Areas C and D are the medium-thickness wall, Area E is the thin wall, and Area F is the flange bottom with a thickness of 6–7 mm. For each part, 4–8 samples with a size of 34 mm×10 mm×1.5 mm were sectioned for the creep rupture life testing.

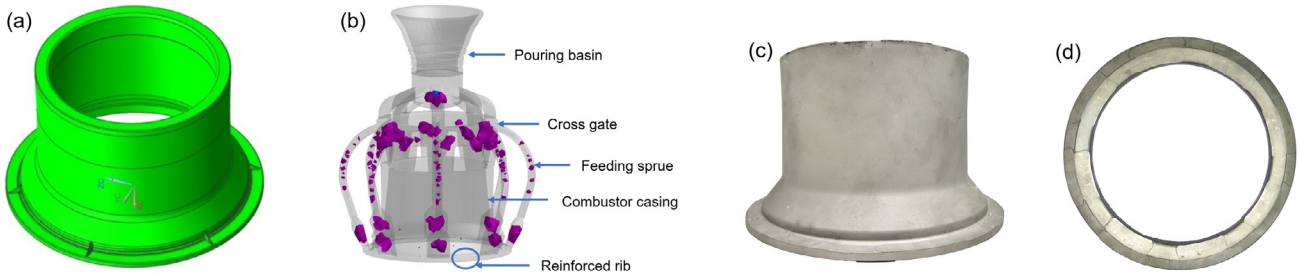


Fig. 1: Drawing of combustion chamber casing simulator (a) and the casting technology^[25] (b) of K439B superalloy, and the view of real casting of combustion casing (c, d)

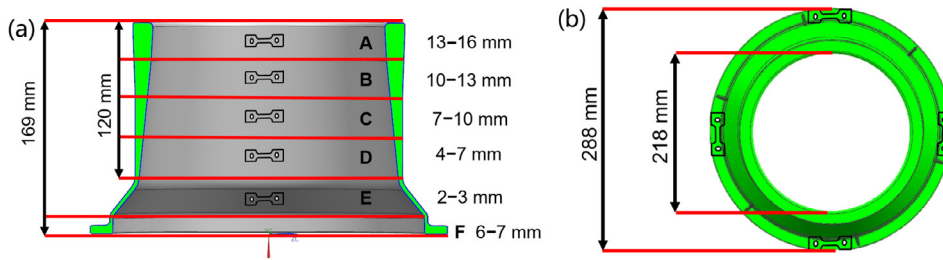


Fig. 2: Sectioning scheme from the casting: front (a) and vertical (b) views of the sectioning position and the size of samples

2.4 Characterization of microstructure and properties

The samples for microstructure observation were prepared using the electrolytic etching method in the solution of $H_3PO_4:HNO_3:H_2SO_4=3:10:12$ to obtain the high-definition γ' phase morphology. The chemical etching was carried out with the solutions of $HCL:H_2O_2=9:1$ and $HNO_3:HF:C_3H_8O_3=1:2:1$, respectively. The former was used to obtain dendrite morphology, and the latter was used for γ' phase data statistics. The microstructure of the samples was analyzed by an Olympus GX71 optical microscope and a Zeiss Supra 55 scanning electron microscope (SEM) in the modes of secondary electron microscopy and backscattering electron. The experimental parameters of a scanning electron microscope were: a voltage of 15 kV, an aperture size of 60 μm , a working distance of 9-11 mm. The composition of the sample was analyzed by EDS. The secondary dendrite arm spacing, the size and volume fraction of the γ' phase were analyzed using the Image-Pro Plus software. The CRL of the samples was tested under the conditions of 815 $^{\circ}C/379$ MPa using a J-30 type high-temperature creep tester, and the samples were tested 4-8 times to obtain the average CRL.

3 Results and discussion

3.1 Strong SSE on creep rupture life

The average CRL tested at 815 $^{\circ}C/379$ MPa in the 6 areas of the casting is shown in Fig. 3. Generally, the CRL of casting decreases with the increase in the wall thickness. The CRL of the casting in Area E reaches up to 114.7 h, while that in Area A is only 45.1 h, a decrease of more than 60%, indicating a strong size effect. In addition, the structure and shape also have an

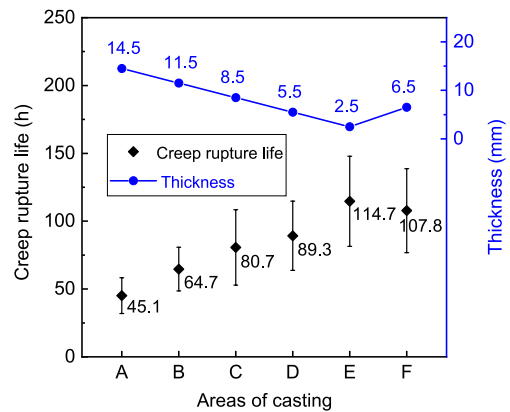


Fig. 3: Creep rupture life of casting in different areas under 815 $^{\circ}C/379$ MPa

important impact on the CRL of the casting. The CRL in Area F is higher than that in Area D, although Area F is thicker than Area D. Furthermore, the CRL in Area F is 33.5% higher than that in Area C, although the upper limit of the thickness of Area F is close to the lower limit of the thickness of Area C, as shown in Fig. 2. These results indicate that the CRL of the casing simulator also has an obvious shape effect. Intuitively, the shape effect is due to the difference in the position where the solidification sequence and feeding ability are different under the conditions of this casting process.

3.2 Cooling rate dependence of CRL

In order to investigate the impact of SSE on the creep rupture life in the context of the solidification process, the cooling rate in various areas of the casting was examined. The cooling rate curves in different regions of the casting obtained using PROCAST software are depicted in Fig. 4(a). It can be observed that the temperature in the solid-liquid region is between 1,299.3

and 1,361.2 °C. The cooling rate of each area decreases with solidification process. Hence, the slope of the solidification curve at the liquidus line is regarded as the effective cooling rate of the casting. The cooling rates in different areas are presented in Fig. 4(b). It can be seen that the maximum cooling rate of the casting reaches up to 18.5 °C·s⁻¹ in Area E, while the lowest cooling rate in Area A is only approximately 1 °C·s⁻¹. The difference in the cooling rates between these two areas is more than one order of magnitude. It is also notable that the cooling rate in Area F reaches up to 10.5 °C·s⁻¹, which is higher than those in Areas C and D. The CRL is closely related to cooling rate, and the claim that only wall thickness and location affect CRL is incomplete.

3.3 Dendrite structure and precipitation phase in different areas of casting

Basically, the variation of the cooling rate in different areas of the casting will result in different microstructures. The dendrite structures of the casting in 6 different areas are shown in Fig. 5. It is obviously observed that the dendrite structures in all 6 areas are thriving. The secondary dendrite arm spacing (SDAS) decreases with the increase of the cooling rate. Among them, the maximum and minimum SDAS are 91 μm and 72.1 μm in Areas A and E, respectively. According to Ref. [27], the relationship between SDAS (λ_2) and the cooling rate (GR) can

be expressed by

$$\lambda_2 = \beta * (GR)^{-1/3} \quad (1)$$

where the coefficient β was calculated to be 27.8 by using the cooling rate in Fig. 4(b) and the average secondary dendrite arm spacing measured in Fig. 5. The cooling rate dependence of λ_2 is shown in Fig. 6. It is seen that the relationship between these two parameters fits Eq. (1) very well.

Considering that precipitation of γ' phase plays a critical role in the high temperature strengthening of the superalloy, the size and volume fraction of γ' phase in different areas were studied using SEM, as shown in Figs. 7 and 8. Most of γ' phases in all the 6 areas take subsphaeroidal shape. A small quantity of γ' phases appear in square rotundity. The dendrite trunk contains only small γ' phase particulate, whereas dual-state γ' phases with small and large size are distributed in interdendritic region. The size of small γ' phase particulates in dendrite trunk is similar to that in interdendritic region. The size and volume fraction distribution of large and small γ' phase particulates in different areas were counted, as shown in Fig. 9. It is obviously seen from Fig. 9(a) that the volume fraction of γ' phase particulates in dendrite trunk increases with the increase of cooling rate, which is opposite to variation tendency of the size of γ' phase. The average size of γ' phase in dendrite trunk is decreased by 36.8% and that in interdendritic

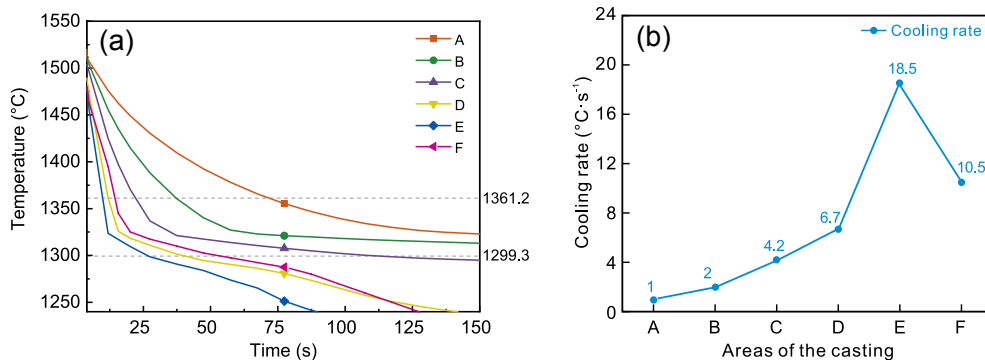


Fig. 4: Cooling rate of castings: (a) cooling curves of the casting in different areas during cast process; (b) cooling rates corresponding to different areas

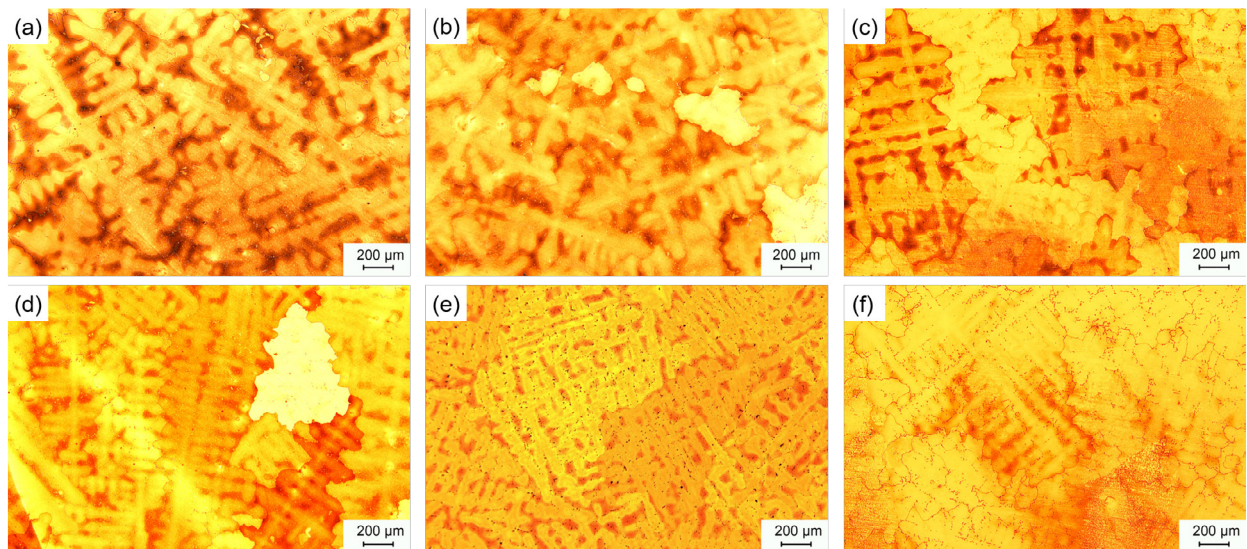


Fig. 5: OM morphologies of dendrites in different areas of casting, (a)-(f) represents Areas A-F, respectively

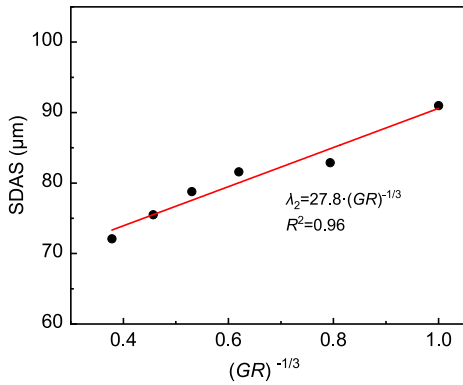


Fig. 6: Relationship between secondary dendrite arm spacing (λ_2) and third root of cooling rate $[(GR)^{-1/3}]$

region is decreased by 30.9%, when compared those in Areas A and E, respectively. The above results of the structural characteristics indicate that the fine dendrite structure, high volume fraction and small size of γ' phase are the main factors to endow superior CRL in Area E.

3.4 Microsegregation in different areas of casting

In casting, microsegregation refers to the difference between the dendrite trunk and the interdendritic regions. The segregation ratio, K , is expressed as:

$$K = C_{dc} / C_{id} \quad (2)$$

where C_{dc} and C_{id} are the element content in dendrite trunk

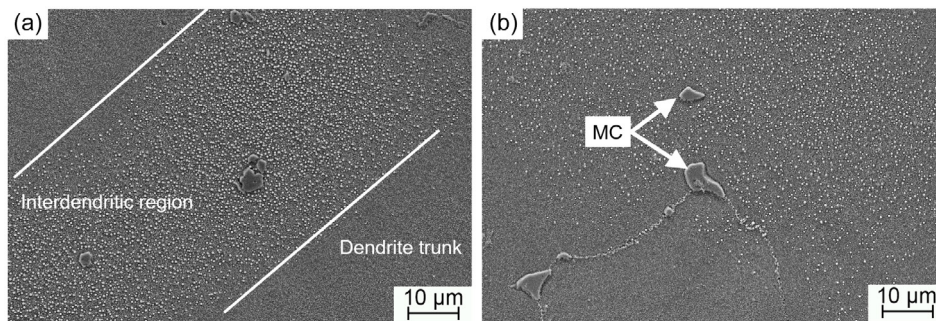


Fig. 7: Typical microstructure of casting showing dual-state γ' phase in interdendritic area (a) and the distribution of carbides (b)

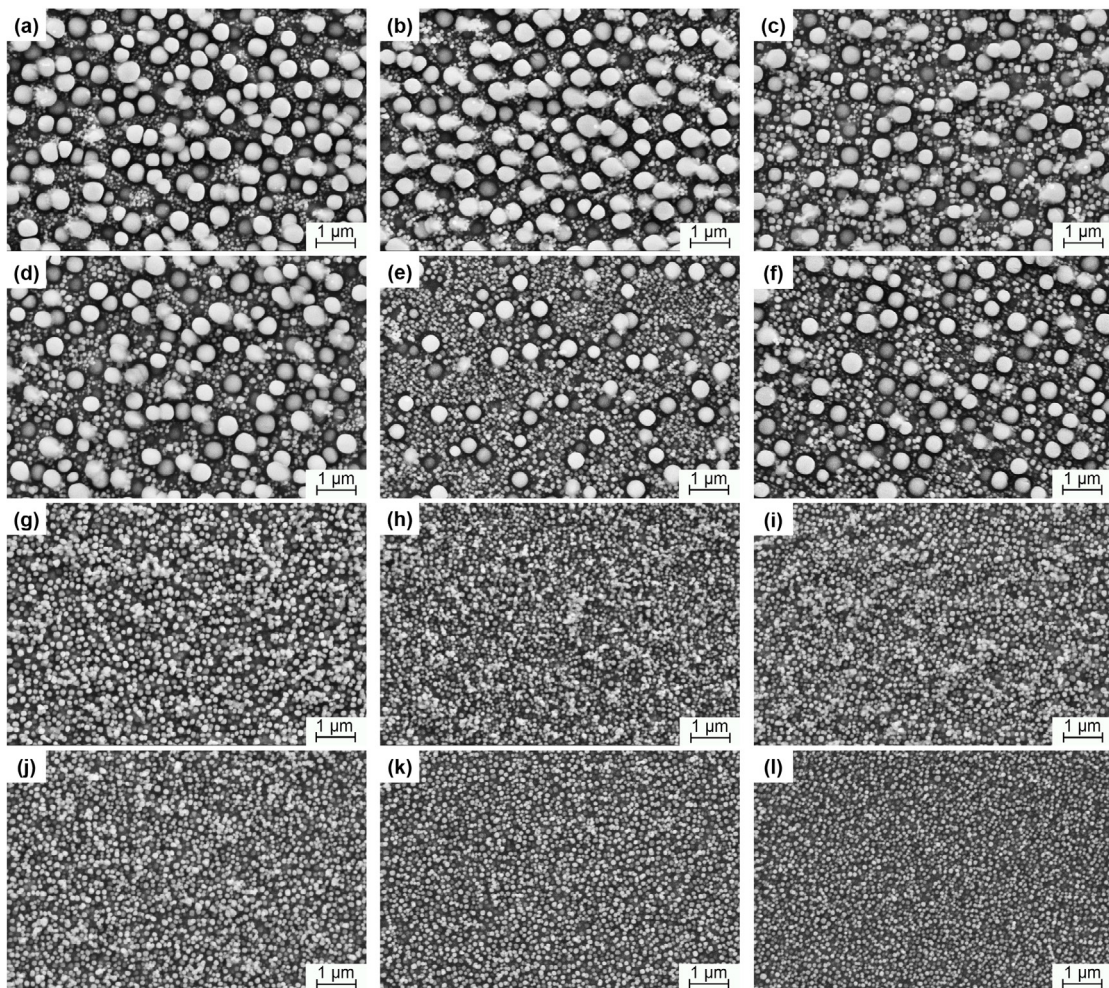


Fig. 8: SEM morphologies of γ' phase in interdendritic region (a-f) and dendrite trunk (g-l), respectively

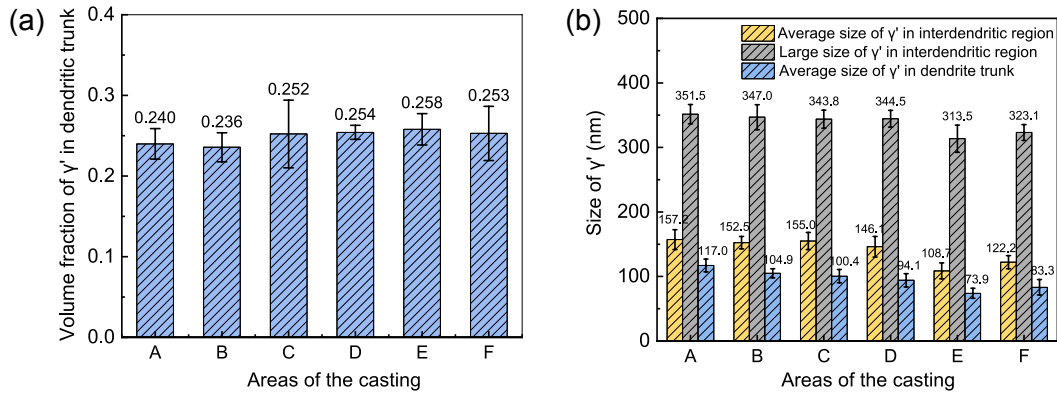


Fig. 9: Volume fraction (a) and size (b) of γ' phase in different areas of the casting

and interdendritic region. Although the casting was processed using heat treatment and HIP, the microsegregation in the casting can be alleviated, it cannot be completely eliminated, which may damage the CRL of the casting. In this work, the microsegregation of each element in different areas was measured using the SEM-EDX method. The microsegregation coefficients of each element in different areas are shown in Fig. 10. It can be seen that the W element shows obvious positive microsegregation, while Ta and Nb show obvious negative microsegregation. The other elements show slight microsegregation. The positive microsegregation of W means that more W atoms in the dendrite trunk can produce a stronger solid solution strengthening (SSS) effect. Regarding the difference in microsegregation in different areas, it can be seen that the microsegregation of the Ta elements in Area E is relatively low among 6 areas. The minimum negative Ta segregation coefficient in Area E among 6 areas indicates that there are fewer Ta atoms in the interdendritic region of Area E, which is also beneficial to SSS and the formation of the γ' phase in the dendrite trunk, compared to those in other areas. This is consistent with the statistics of the content of γ' phase at the dendritic trunk in each region in the previous section: the content of γ' phase at the dendritic trunk in Area E is the highest among all regions, reaching 25.8%. It is noted that the microsegregation of Nb in Area E is not the minimum, indicating that the segregation of Nb is not only affected by the cooling rate, but also by the formation of carbides, heat treatment, and HIP processes. Therefore, it is the positive

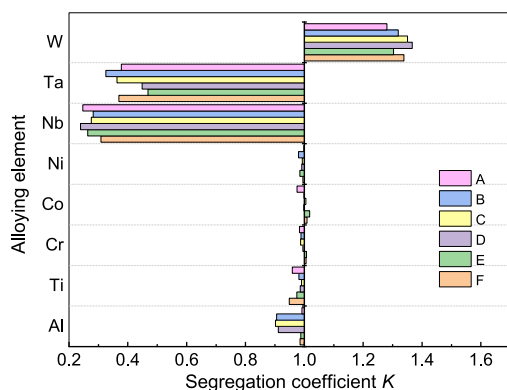


Fig. 10: Segregation coefficient K between dendrite trunk and interdendritic regions in different areas of casting

microsegregation of W in the dendrite trunk and the minimum microsegregation of Ta in the interdendritic region of Area E that result in the enhanced SSS effect in Area E.

Based on the above results, the CRL of the casting is strongly affected by the wall thickness and position, and the cooling rate is well correlated with the CRL. The SSE is actually attributed to the cooling rate and solidification sequence under the casting process conditions. The variation of the cooling rate in different areas of the casting leads to different SDAS. The relationship between SDAS and the cooling rate fits the classical dendrite growth equation very well. Furthermore, the sizes of both large and small γ' phase particles decrease with the increase of the cooling rate, and the volume fraction of γ' phase particles in the dendrite trunk increases with the increase of the cooling rate. The structural characteristics indicate that the fine dendrite structure, high volume fraction, and small size of the γ' phase are the main factors to confer superior CRL. The W element shows obvious positive microsegregation, while Ta and Nb show obvious negative microsegregation in the part with the highest cooling rate. The positive microsegregation of W and the minimum negative Ta segregation coefficient in the interdendritic region is beneficial to SSS and the formation of the γ' phase in the dendrite trunk, which may contribute to the improvement of CRL.

4 Conclusions

(1) For the combustion chamber casing simulator made of K439B superalloy, there is a significant size and shape effect on creep rupture life, meaning that the creep rupture life is highly dependent on the wall thickness and structure of the casing. Specifically, the maximum difference in creep rupture life values in different areas can reach up to 60%.

(2) The impact of the size and shape effect on creep rupture life is actually related to the cooling rate in different areas, while the cooling rate is determined by the casting shape and solidification conditions. The creep rupture life of the area with a high cooling rate is longer, and as the cooling rate decreases, the creep rupture life gradually shortens. In terms of casting technology, the creep rupture life in different areas is mainly affected by the cooling rate rather than just the wall thickness or structure of the casting.

(3) The impact of the size and shape effect on creep rupture life can be explained by the microstructure features. The secondary dendrite arm spacing is inversely proportional to the cube root of the cooling rate, which satisfies the classical dendrite growth theory. With the increase of the cooling rate, the volume fraction of γ' phase in the dendrite trunk increases, but the size shows a downward trend. The maximum difference in the size of the γ' phase in the dendrite trunk in different areas can reach up to 36.8%. The microstructure changes in different areas are mainly affected by the cooling rate. Different dendritic structures, volume fractions and sizes of γ' phase are also the main factors for the change of creep rupture life in the 6 areas of the casing simulator.

(4) The change of the cooling rate directly affects the solute distribution of W and Ta during solidification. W shows positive microsegregation in the dendrite trunk, and Ta shows the minimum negative Ta segregation coefficient in Area E among the 6 areas, which is beneficial to solid solution strengthening and the formation of the γ' phase in the dendrite trunk.

Acknowledgments

This work was financially supported by the National Science and Technology Major Project of China (No. J2019-VI-0004-0117), and a Laboratory Fund Project (6142903220101).

Conflict of interest

The authors declare that they have no known competing financial interests or personal relationships that could have appeared to influence the work reported in this paper.

References

- [1] Pollock T M. Alloy design for aircraft engines. *Nature Materials*, 2016, 15(8): 809–815.
- [2] Singh K. Advanced materials for land based gas turbines. *Transactions of the Indian Institute of Metals*, 2014, 67(5): 601–615.
- [3] Ren R, Ma X Y, Yue H H, et al. Stiffness enhancement methods for thin-walled aircraft structures: A review. *Thin-Walled Structures*, 2024: 111995.
- [4] Wu J J, Meng J, Zou M K, et al. Effect of wall thickness on micropores and stress-rupture properties of a single-crystal nickel-based superalloy. *Materials Science and Engineering: A*, 2023, 872: 144941.
- [5] Xu H Y, Huang T W, Ai C, et al. Effect of thickness on microstructure of thin-walled nickel-based single-crystal superalloy castings. *Journal of Materials Research and Technology*, 2024, 29: 2912–2917.
- [6] Nawrocki J, Motyka M, Szeliga D, et al. Effect of cooling rate on macro-and microstructure of thin-walled nickel superalloy precision castings. *Journal of Manufacturing Processes*, 2020, 49: 153–161.
- [7] Harris K, Erickson G, Schwer R. Directionally solidified and single-crystal superalloys. *Metals Handbook*, 1990: 995–1006.
- [8] Fourie J, Baldan A. Size effects in the mechanical properties of superalloy single crystals. TMS: Philadelphia, PA, USA, 1992: 619–627.
- [9] Reed R. The superalloys: Fundamentals and applications. The Edinburgh Building: Cambridge University Press, 2006: 1–372.
- [10] Gudivada G, Pandey A K. Recent developments in nickel-based superalloys for gas turbine applications: Review. *Journal of Alloys and Compounds*, 2023, 963: 171128.
- [11] Detrois M. Advancing development and application of superalloys. *JOM*, 2020, 72(5): 1783–1784.
- [12] Anbarasan N, Gupta B K, Prakash S, et al. Effect of heat treatment on the microstructure and mechanical properties of Inconel 718. *Materials Today: Proceedings*, 2018, 5(2): 7716–7724.
- [13] De Bartolomeis A, Newman S T, Jawahir I S, et al. Future research directions in the machining of Inconel 718. *Journal of Materials Processing Technology*, 2021, 297: 117260.
- [14] Zhang Z, Wang R, Lv Y T, et al. Microstructures and mechanical properties of heat treated TiC/GTD222 nickel-based composite prepared by selective laser melting. *Materials Science and Engineering: A*, 2022, 851: 143588.
- [15] Ahmed S, Biswas A N. René 41 & waspaloy based comparative study for high pressure turbine blades used in turboshaft engines. *Materials Today: Proceedings*, 2022, 56: 1234–1241.
- [16] Lancaster R, Davies S, Jeffs S, et al. The effects of thermal exposure on the high temperature behaviour of a laser powder bed fused nickel based superalloy C263. *Materials Science and Engineering: A*, 2021, 801: 140409.
- [17] Wu S J, Shao L, Li Z P. Effects of service thermal cycles on the microstructure and mechanical property of K4648 superalloy. *Journal of Alloys and Compounds*, 2016, 683: 533–541.
- [18] Liu Y, Wu D T, Gao Z H, et al. Influence of cold metal transfer welding parameters on the welding hot crack of Mar-M247 nickel-based superalloy. *Journal of Materials Research and Technology*, 2024: 6341–6354.
- [19] Sjöberg G, Imamovic D, Gabel J, et al. Evaluation of the IN939 alloy for large aircraft engine structures. *Superalloys*, 2004: 441–450.
- [20] Wahl J B H K. CM939 weldable[®] alloy update, ASME ASME Turbo Expo 2007: Power for land, sea, and air. In: ASMEDC, Montreal, Canada, 2007, 47942: 35–42.
- [21] Chen J, Ren X, Zhang M, et al. Microstructure and typical properties of cast Ni-based superalloy K439B. *Heat Treatment of Metals*, 2023, 48(1): 100–104. (In Chinese)
- [22] Men D, Li G. Characterization of laser welded joint of K439B alloy: A methodological study. *Chinese Journal of Vacuum Science and Technology*, 2020, 40(7): 697–701. (In Chinese)
- [23] Zhang L L, Chen J Y, Tang X, et al. Evolution of microstructures and mechanical properties of K439B superalloy during long-term aging at 800 °C. *Acta Metallurgica Sinica*, 2023, 59(9): 1253–1264. (In Chinese)
- [24] Gao L, Qu X, Wu Y, et al. Evolution of carbides in K439B nickel-based cast superalloy during long-term aging at 800 °C. *Materials Reports*, 2024: 1–13. (In Chinese)
- [25] Zheng B Y, Wu Y D, Chen J Y, et al. Predication of the defects and optimization of the technology for the investment casting of thin-wall experimental cartridge receiver made of K439B superalloy. *Foundry Technology*, 2023, 44(2): 147–152. (In Chinese)
- [26] Luo A A, Sachdev A K, Apelian D. Alloy development and process innovations for light metals casting. *Journal of Materials Processing Technology*, 2022, 306: 117606.
- [27] Hoó C, Teleszky I, Roósz A, et al. Estimation of the cooling rate on the basis of secondary dendrite arm spacing in case of continuous cast steel slab. *Materials Science Forum*, 2006, 508: 245–250.